POLITECNICO DI TORINO
Repository ISTITUZIONALE

Symmetric Short-Circuit Model of Synchronous Machines based on Flux and Loss Maps

Original
Symmetric Short-Circuit Model of Synchronous Machines based on Flux and Loss Maps / Ferrari, S., Bojoi, A., Mirazimi, M., Pescetto, P., Ronchetto, D., Cagnetta, P., Pellegrino, G.. - ELETTRONICO. - (2024), pp. 5056-5063. (2024 IEEE Energy Conversion Congress and Exposition (ECCE) Phoenix, AZ, USA 20-24 October 2024) [10.1109/ecce55643.2024.10861274].

Availability:
This version is available at: 11583/2998161 since: 2025-03-07T14:30:58Z

Publisher:
IEEE

Published
DOI:10.1109/ecce55643.2024.10861274

Terms of use:

This article is made available under terms and conditions as specified in the corresponding bibliographic description in the repository

Publisher copyright
IEEE postprint/Author's Accepted Manuscript

©2024 IEEE. Personal use of this material is permitted. Permission from IEEE must be obtained for all other uses, in any current or future media, including reprinting/republishing this material for advertising or promotional purposes, creating new collecting works, for resale or lists, or reuse of any copyrighted component of this work in other works.

(Article begins on next page)

21 November 2026

Symmetric Short-Circuit Model of Synchronous Machines based on Flux and Loss Maps

Simone Ferrari*, Andrei Bojoi*, Maedeh Mirazimi*, Paolo Pescetto*
Davide Ronchetto†, Paolo Cagnetta‡, Gianmario Pellegrino*
*Energy Department "Galileo Ferraris",Politecnico di Torino, Turin, Italy
† Controls, Accessories and Marine, Avio Aero, Rivalta di Torino, Italy
‡ Controls, Accessories and Marine, Avio Aero, Bari, Italy
Emails: simone.ferrari@polito.it, andrei.bojoi@polito.it, maedeh.mirazimi@polito.it, paolo.pescetto@polito.it
davide.ronchetto@avioaero.it, paolo.cagnetta@avioaero.it, gianmario.pellegrino@polito.it

***Abstract*—The peak current during a short-circuit is a crucial performance index for Permanent Magnet Synchronous Motors (PMSMs). This indicator is even more critical for propulsion applications since the Active Short-Circuit (ASC) is one of the most common reaction strategies triggered when a system failure is detected, both for terrestrial and aerospace systems. Because of the non-linear behaviors of high-performance PMSMs and the trend towards rare-earth free Permanent Magnets (PMs) for traction applications, the peak current during ASC must be accurately evaluated, avoiding excessive oversizing but still guaranteeing the health of the PMs after the fault. In this paper, a fast and accurate model to compute the instantaneous current and torque during ASC is presented. The proposal relies on flux and loss maps, directly accounting for saturation and cross-saturation phenomena and also the iron and AC loss, typically neglected in the existing models. The proposed methodology is exploited to assess the performance of a double three-phase PMSM designed for aerospace applications. The two AC loss components, namely iron loss and loss related to skin and proximity effect in the winding, are considered and the effect of each of them is highlighted. Then, the proposed maps elaboration is compared with the dynamic model in Simulink/SimScape and against dedicated Finite Element Analysis (FEA) simulations.**

***Index Terms*—Electrical Machines, Permanent Magnet Synchronous Machines, Active Short-Circuit**

I. Introduction

Nowadays, Permanent Magnet Synchronous Machines (PMSMs) are among the most adopted motors for electric propulsion in several transportation scenarios [1]–[4], offering high torque and power density thanks to the rotor anisotropy and the Permanent Magnets (PMs) presence. Besides these advantages, the PMs' presence poses a risk in case of inverter failure at high speed, possibly inducing harmful voltages that can damage the inverter and battery [5], [6]. To avoid that, the most adopted reaction is the Active Short-Circuit (ASC), which is triggered by the system controller if a system fault is detected [7], [8]. Thanks to this strategy, the electrical part of the powertrain and the passengers are safe, but the motor can be irreversibly demagnetized due to the uncontrolled current transient [9]. This problem is even more critical if non-rare-earth PMs are adopted (as ferrites or other innovative materials), which presents low coercivity. Furthermore, the torque undulation during the ASC transient can be harmful to the mechanical system integrity and in steady-state a breaking torque is always generated. For these reasons, an accurate estimation of current during ASC is crucial to avoid unnecessary motor oversizing. One example for aerospace application of this kind of motor and problems is studied for the AVALON project, that is a cooperative project PON-MUR (managed by the Italian ministry of university) launched in 2019 and that put together expertize from university and industry and has the aim of developing sustainable aerospace propulsion systems. The motor models adopted for ASC computation typically rely on linear formulations, that are inaccurate for propulsion PMSMs, normally designed to operate up to deep magnetic saturation because of the high power density requested. On the other side, Finite Element Analysis (FEA) models can be coupled with circuital models, allowing higher accuracy but also longer computational time. A trade-off between these two approaches is the use of saturation maps in the analytical model [10], including the saturation and cross-saturation modeling. Still, the saturation maps are a static representation of the machine behavior. Therefore, the rotational loss, namely iron loss, PM loss, and AC winding loss, are neglected in the literature, while they can affect the ASC transient.

This paper extends the model presented in [10] by adding the rotational loss in the short-circuit computation, both in the steady-state model and in the transient model. The iron loss is included through the iron and PM loss map, while the winding AC loss factor is modeled with time-harmonic FEA simulations and mapped over a temperature-frequency domain. The loss modeling approach is described in [11].

To demonstrate the methodology and validate it, a double three-phase PMSM for aerospace application is considered.

TABLE I
Benchmark Motor Ratings

Number of pole pairs		5
Number of slots		60
Number of phases		6
Maximum torque	(Nm)	128
Base speed	(rpm)	12000
Maximum speed	(rpm)	18000
Peak power	(kW)	150
Peak phase current	(Apk)	300
DC-link voltage	(Vdc)	390

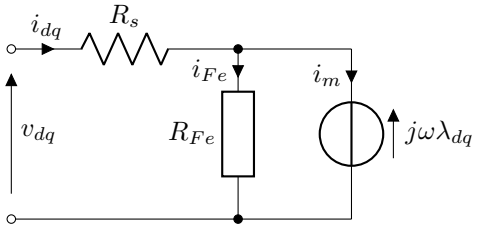


Fig. 1. Equivalent circuit of the dq motor model.

The motor is designed for fault-tolerant application, meaning that the demagnetization limit is far from the fault conditions, even at high temperatures and the no-load voltage is below the rated voltage even at overspeed. Furthermore, one of the design specifications is the possibility to thermally survive to the short-circuit both in transient and in steady-state. Thanks to this intrinsic safety, this design is a perfect candidate to validate the methodology experimentally. Furthermore, the selected prototype features high-speed operation (the base speed at 12 krpm and maximum speed at 18 krpm), making the estimation of rotational loss relevant. The motor is equipped with hairpin winding, which further increases the effect of the speed on the loss components. The ratings of the motor are reported in Tab I.

The two models presented in the following (for steady-state and transient short-circuit computation) are then included in SyR-e [12], sharing the developed processes with the scientific and industrial community.

II. Motor Model Review

The electric model of a generic PMSM can be expressed as;

$$v_{dq} = R_s \cdot i_{dq} + j \cdot \omega\lambda_{dq} + \frac{d\lambda_{dq}}{dt} \tag{1}$$

where R_s is the phase resistance, v_{dq} is the phase voltage in the dq frame, i_{dq} is the phase currents, λ_{dq} is the dq flux linkages, j is the complex operator and ω is the electric pulsation, defined as:

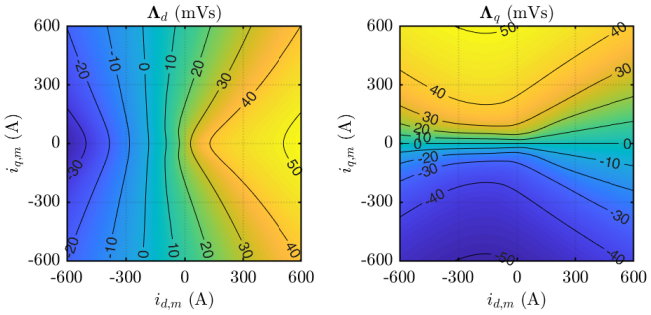
$$\omega = n \cdot \frac{\pi}{30} \cdot p \tag{2}$$

from the rotor speed n and the pole pair number p. Note that for compactness, the dq complex notation $x_{dq} = x_d + j \cdot x_q$ is adopted. The electric model is described alternatively from the circuit reported in Fig. 1.

The phase current i_{dq} is obtained by the sum of the magnetizing components $i_m = i_{d,m} + j \cdot i_{q,m}$ and the component related to iron and PM loss $i_{Fe} = i_{d,Fe} + j \cdot i_{d,Fe}$.

while the dq components of the flux linkage are conveniently modeled through flux maps. Assuming that $\mathbf{\Lambda}_d$ and $\mathbf{\Lambda}_q$ are the d and q axis flux linkage maps, function of the magnetizing current, the flux linkages of the motor for (1) can be computed as:

$$\begin{cases} \lambda_d = \mathbf{\Lambda}_d(i_{d,m}, i_{q,m}) \\ \lambda_q = \mathbf{\Lambda}_q(i_{d,m}, i_{q,m}) \end{cases} \tag{3}$$



(a) (b)

Fig. 2. Flux maps of the benchmark motor computed at $\Theta_{PM} = 120°$C.

Please note that in the following, capital bold fonts will identify generic maps (also in complex form) that are expressed the function of the dq magnetizing currents. The flux maps of the benchmark motor are reported in Fig. 2. Thanks to the flux maps representation, all the PMSMs can be modeled and the Synchronous Reluctance Motors (SyRMs) are included in this framework, as can be seen in PMSMs with high anisotropy and null PM flux linkage.

A. Iron and PM Loss Model

Iron and PM loss are modeled similarly. Assuming sinusoidal currents, the iron loss is mapped over the $(i_{d,m}, i_{q,m})$ domain at a constant speed of n_0. The iron loss is modeled using the improved Generalized Steinmetz equations (iGSE), with the additional term of the eddy current loss:

$$p_{Fe} = k_h \cdot f^\alpha \cdot B^\beta + k_e \cdot (f \cdot B)^2 \tag{4}$$

where k_h, k_e, α and β are loss coefficients fitted from the loss curves of the material, f is the fundamental frequency and B is the flux density. The PM loss are function of the eddy currents and so are proportional to f^2. The iron and PM loss map $\mathbf{P}_{Fe}$ is then computed as:

$$\mathbf{P}_{Fe} = \mathbf{P}_{h,0} \cdot \left(\frac{n}{n_0}\right)^\alpha + (\mathbf{P}_{e,0} + \mathbf{P}_{PM,0}) \cdot \left(\frac{n}{n_0}\right)^2 \tag{5}$$

Where $\mathbf{P}_{h,0}$, $\mathbf{P}_{e,0}$ and $\mathbf{P}_{PM,0}$ are the maps of hysteresis loss, eddy current loss, and PM loss, respectively computed at the speed n_0 and n is the generic speed. As for the previously defined notation, all these maps are functions of the magnetizing currents, even if it is not explicitly written for space reasons. Further details can be found in [11]. From the iron and PM loss map, the equivalent current that flows in the parallel branch is computed as:

$$\mathbf{I}_{Fe} = \left[\frac{2}{3} \cdot \mathbf{P}_{Fe} \oslash (j \cdot \omega \cdot \mathbf{\Lambda}_{dq})\right]^* \tag{6}$$

This map will allow us to retrieve the i_{Fe}, given the magnetizing current. As an example, the iron and PM loss maps and the map of the equivalent current are reported in Fig. 3 for the motor base speed. Note that $|\mathbf{I}_{Fe}|$ values are quite low compared to the magnetizing current.

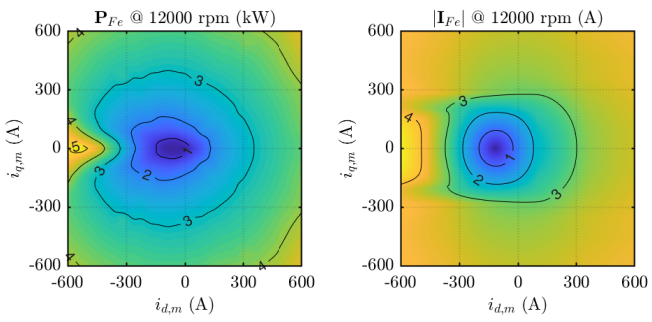


Fig. 3. a) Iron and PM loss map and b) map of the current equivalent to iron loss for the benchmark motor, computed at $\Theta_{PM} = 120°$C and 12000 rpm.

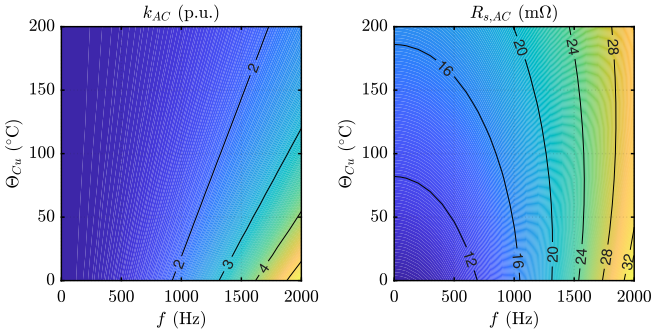


Fig. 4. AC loss factor model: a) computed AC loss factor and b) phase resistance of the benchmark motor function of frequency and winding temperature.

B. AC-related Copper Loss

The effect of AC current on the copper loss is crucial for hairpin windings. Indeed, this kind of conductors offers higher slot filling factor compared to stranded winding, but the bigger cross-section of the conductors increase the skin and proximity effect, creating uneven current density distribution in the conductor and ultimately increasing the copper loss. To model this behavior, the AC loss factor k_{AC} is computed by means of time harmonic FEA simulations over a map of frequency and copper temperature, as reported in Fig. 4a.

It must be remarked that the AC loss factor computed by FEA simulations refers to the slot section only and not for the end-windings. For the latter, the modeling is more critical since there is a transposition of the conductors, welding points, and jumpers. The AC factor can be defined also in this area but typically results drastically lower than in the active section, for this reason, it will be neglected in the following. The AC phase resistance is then computed as:

$$R_s = R_{s,DC} \cdot \left[k_{AC}(\Theta_{Cu}, f) \cdot \frac{L}{L + L_{ew}} + \frac{L_{ew}}{L + L_{ew}} \right] \quad (7)$$

where R_s is the phase resistance with AC effects computed at the temperature Θ_{Cu} and the frequency f, $R_{s,DC}$ is the phase resistance at the temperature Θ_{Cu} and in DC conditions ($f = 0$ Hz), L is the stack length and L_{ew} is the end-winding length. The map of phase resistance is reported in Fig. 4. It is worth noting that for low frequency, the resistance increases linearly with temperature, as expected. Indeed, for high frequency, the behaviors of AC loss factor with temperature make the resistance less sensitive to temperature. The copper loss is then computed as:

$$P_{Cu} = \frac{3}{2} \cdot R_s \cdot |i_{dq}|^2 \quad (8)$$

III. Steady-State Short-Circuit Solution

First of all, the Steady-State Short-Circuit (SSSC) condition is studied. In this case, the results are steady state current and braking torque function of the motor speed. Starting from the electric model (1), the derivative terms become zero and the voltage, current, and flux linkage maps are adopted instead of the single values, resulting in:

$$\mathbf{V}_{dq} = R_s \cdot \mathbf{I}_{dq} + j \cdot \omega \mathbf{\Lambda}_{dq} \quad (9)$$

The SSSC operating point is found over the $(i_{d,m}, i_{q,m})$ plane identifying the operating point that presents $v_d = v_q = 0$. For each operating speed, the computation steps are:

1) Compute the fundamental frequency f as:
$$f = \frac{n}{60} \cdot p \quad (10)$$
2) Phase resistance is computed at the considered frequency and winding temperature with (7);
3) The map of equivalent current for iron and PM loss $\mathbf{I}_{Fe}$ is computed at the fundamental frequency;
4) The total current map (in complex coordinates) is computed as:
$$\mathbf{I}_{dq} = \mathbf{I}_m + \mathbf{I}_{Fe} \quad (11)$$
5) The phase voltage map in the dq frame is computed with (9);
6) The point $v_{dq} = 0$ is identified in the voltage maps by intersecting the curves $v_d = 0$ and $v_q = 0$.

The graphical process of SSSC operating point identification is reported in Fig. 5 for 180 rpm and 18000 rpm (maximum

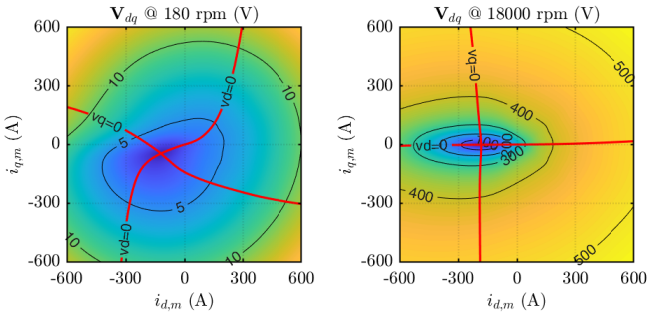


Fig. 5. Voltage maps at a) 180 rpm and b) 18000 rpm with the lines for the SSSC point identification reported in red.

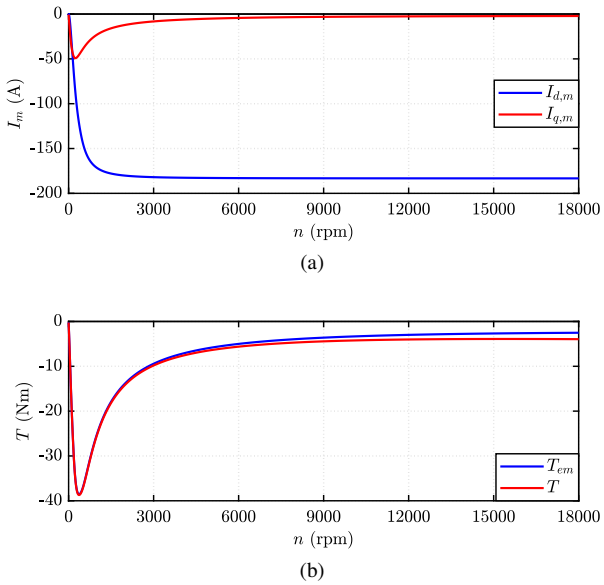


Fig. 6. Results of the SSSC model: a) magnetizing current components and b) torque versus motor speed .

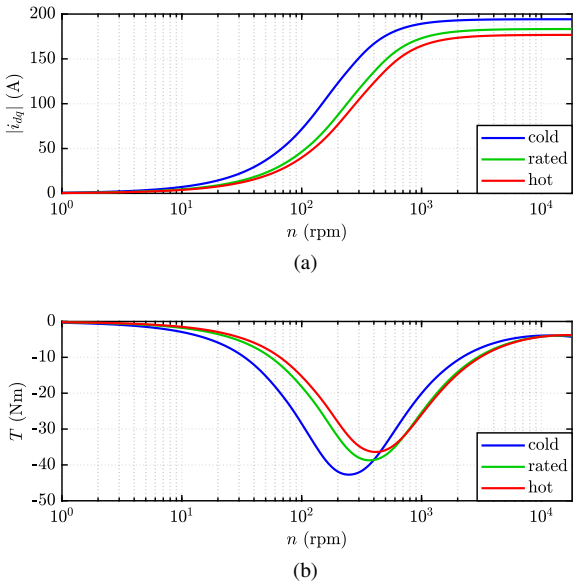


Fig. 7. Effect of temperature on the SSSC: a) current amplitude and b) torque versus speed at three different temperature conditions.

speed). The contours at $v_d = 0$ and $v_q = 0$ are highlighted in red, and the operating point in SSSC conditions over the $(i_{d,m}, i_{q,m})$ plane is identified at the crossing of the two contours.

The results of the SSSC model from zero speed to the maximum motor speed are reported in Fig. 6. The figure reports the magnetizing current components and the braking torque. The total current is almost superimposed on the magnetizing component, because of the low value of the current equivalent to iron loss. Details on loss components will be disclosed later.

The curves are in accordance with the expected shapes: at high speed the braking torque is almost null, and the magnetizing current is aligned against the PM flux linkage ($i_q \cong 0$) and with the amplitude equal to the characteristic current, while at low speed there is a point (around 180 rpm) where the q axis current is non zero and the braking torque has its peak. A last interesting point is evident in the braking torque and the comparison between the electromagnetic torque T_{em} and the mechanical torque T, that also includes the iron loss effects. The electromagnetic torque tends to zero as it increases speed, while the mechanical braking torque is slightly higher in amplitude because of the loss growth, associated with iron loss.

A. *Effect of Temperature*

The effect of temperature is considered for both windings and PMs. The temperature effect on PMs is limited for this motor because of the SmCo PMs, but a minor reduction in the PM remanence causing a slight reduction of the SSSC current at high speed. Regarding the windings, the temperature affects both the DC resistance, increasesing it proportionally with the temperature rise, but the AC factor is reduced because of the higher resistivity. Three temperature conditions are considered in the following, as reported in Tab. II. Fig. 7 reports the steady-state torque and current amplitude as a function of speed for the three considered motors. The speed axis is reported on a logarithmic scale to highlight the differences. First of all, the effect of the different PM remanence is evident when considering the current at high speed (above 1000 rpm, for this motor), where the phase resistance effect is not significant. The current (that is well approximated with the characteristic current) decreases with temperature, as expected from the material characteristics. The effect of the different resistance is evident in the low speed region, where the braking torque is higher. The speed of the maximum braking effect slightly increases with speed, indicating a different weight of the voltage drop over the phase resistance.

The different weight of the resistance is highlighted when considering the loss. Fig. 8 reports the loss components in the three cases as a function of speed. While iron and PM losses are almost insensitive to temperature and increase with speed, copper loss has a more interesting behavior. At low speed but above 1000 rpm, when the phase current is very close to the asymptotic value, the AC effect is low, and the difference is mainly due to the temperature effect on the DC resistance. As speed (and frequency) increase, the AC effect becomes relevant, but since the AC factor is higher at low temperatures, the copper loss is higher for the cold condition. This results in the counter-intuitive behavior of having higher copper loss at cold temperature, for SSSC high speed operations. A final

TABLE II
TEMPERATURE CONDITIONS

	Θ_{Cu} (°C)	Θ_{PM} (°C)
cold	20	20
rated	150	120
hot	200	180

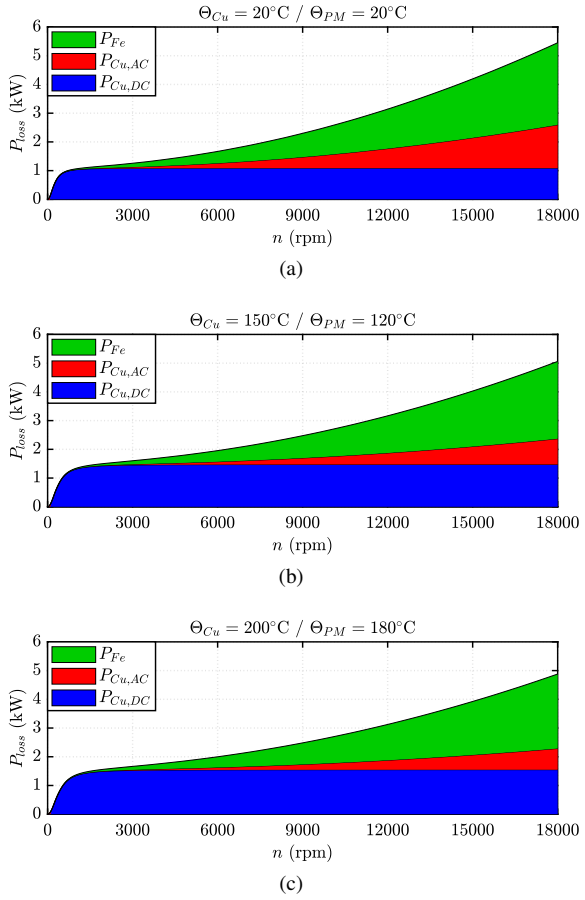


Fig. 8. Effect of temperature on the SSSC versus speed in a) cold, b) rated and c) hot conditions.

comment should be made on the loss distribution. At low speeds, the DC resistance can model the motor behavior with good accuracy. However, as speed increases, the rotating loss becomes relevant and even dominant, when cold condition is considered.

B. Comparison with DC Loss Model

To highlight the impact of the AC, iron and PM loss in the SSSC estimation, the SSSC model is computed with all the loss components enabled and only with the loss related to the DC resistance enabled (as presented in [10]). Fig. 9 reports the differences in torque, phase current and loss between the complete model and the DC-loss-only model. Besides the loss difference, which is evident at high speeds as highlighted in the previous comparison, the main difference is in the torque value. Indeed, neglecting the rotational loss results in a slightly lower braking torque. This difference is evident at high speeds, where rotational losses are higher and the SSSC torque is low. At maximum speed, the additional braking torque is around 2 Nm, that represents 3/4 of the total braking torque at this speed. Regarding the current, the effect is limited and negligible.

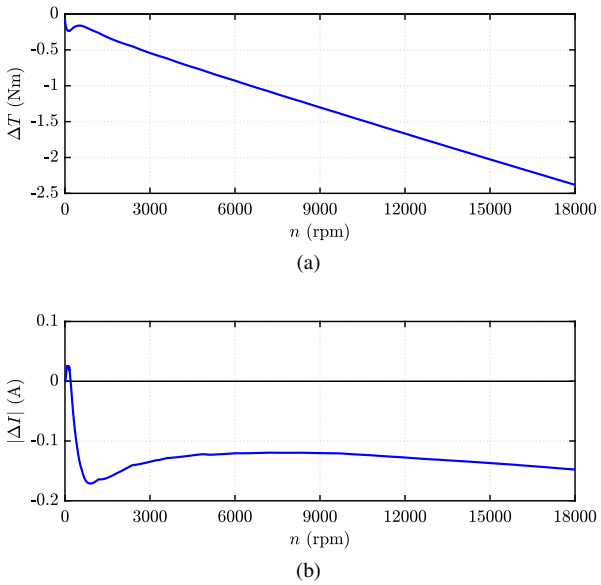


Fig. 9. Effect of AC winding resistance and iron and PM loss on the SSSC: a) torque difference and b) current amplitude difference versus speed.

IV. Transient Short-Circuit Solution

Some of the main issues related to short-circuit refers to the short-circuit transient. Indeed, in a short time frame, high currents are circulating in the motor, posing the risk of irreversible PM demagnetization, and high oscillating torques are induced at the shaft, risking mechanical damages to the driveline. To model the Transient Short-Circuit (TSC) behaviors, the starting point is still the motor model (1). In this case, the derivative terms cannot be deleted, but the voltage components are still set to zero for the short-circuit condition. Before solving the TSC model, the phase resistance R_s at the considered temperature and frequency, and the iron and loss maps $\mathbf{P}_{Fe}(i_{d,m}, i_{q,m})$ at the considered speed must be computed, as well as the map of equivalent current $\mathbf{I}_{Fe}$. To solve the differential equation, the electric model is turned into discrete form and the Euler method is adopted. The speed is kept constant for simplicity. This assumption is justified since the TSC model is intended to model the peak currents, which occur in the very first instants of the short-circuit, when the motor and system inertia keep the rotational speed almost constant. After discretization and transformation, the voltage equations are:

$$\begin{cases} \lambda_d^{k+1} = \lambda_d^k + \left(-R_s \cdot i_d^k + \omega \cdot \lambda_q^k\right) \cdot \Delta t \\ \lambda_q^{k+1} = \lambda_q^k + \left(-R_s \cdot i_q^k - \omega \cdot \lambda_d^k\right) \cdot \Delta t \end{cases} \tag{12}$$

Where, the superscripts k and $k+1$ indicate the current and next time instants, while Δt is the time interval between the two considered instant. The component form of the equation is preferred to the complex form for clarity. Once the flux linkage at the $k+1$ time instant is known, the magnetizing current at $k+1$ is obtained from the inverse model, as follows:

$$\begin{cases} i_{d,m}^{k+1} = \Re\left(\mathbf{I}'_m(\lambda_d^{k+1}, \lambda_q^{k+1})\right) \\ i_{q,m}^{k+1} = \Im\left(\mathbf{I}'_m(\lambda_d^{k+1}, \lambda_q^{k+1})\right) \end{cases} \tag{13}$$

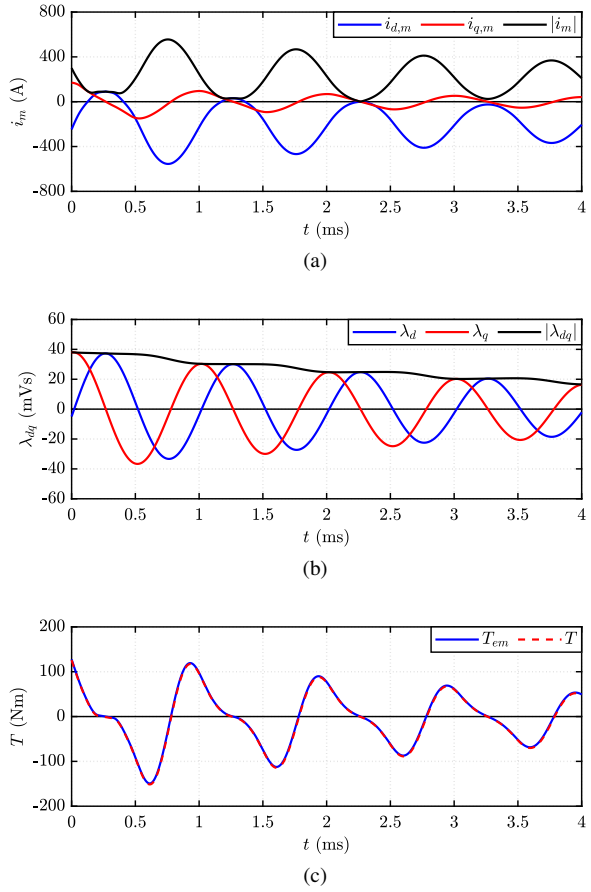


Fig. 10. TSC results at 12000 rpm and from the maximum current: a) magnetizing current components, b) flux linkages and c) torque for 4 periods after the short-circuit trigger.

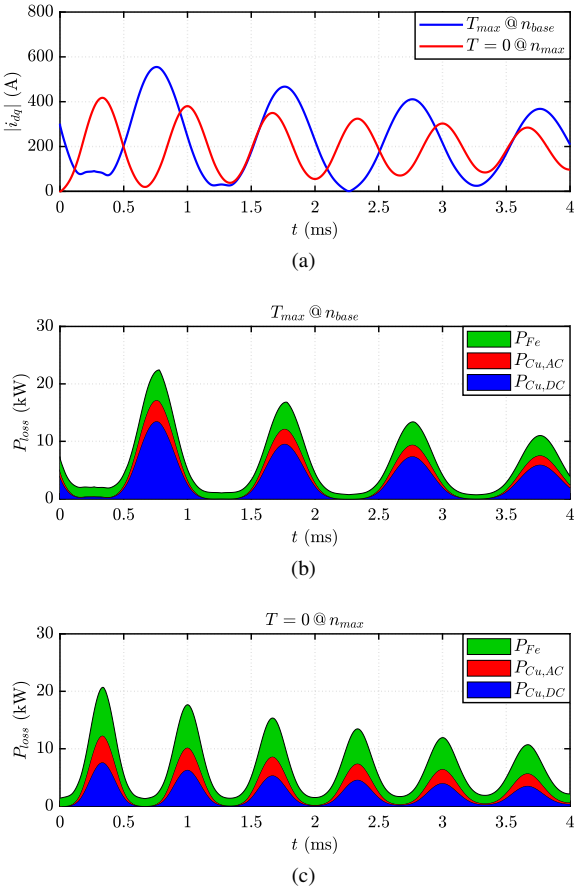


Fig. 11. Effect of pre-fault conditions on TSC behaviors in two operating points: maximum torque at base speed and zero torque at no load. a) current waveform comparison, b) loss segregation for maximum torque point and c) loss segregation for maximum speed point.

where $\mathbf{I}'_m$ is the map of magnetizing currents as a function of the dq flux linkage, obtained from the inversion of flux maps. Once the magnetizing currents are known, all the other quantities can be obtained by interpolating the respective maps. First of all, the current representing the iron and PM losses is computed at the time instant $k+1$ as:

$$\begin{cases} i_{d,Fe}^{k+1} = \Re\left(\mathbf{I}_{Fe}(i_{d,m}^{k+1}, i_{q,m}^{k+1})\right) \\ i_{q,Fe}^{k+1} = \Im\left(\mathbf{I}_{Fe}(i_{d,m}^{k+1}, i_{q,m}^{k+1})\right) \end{cases} \tag{14}$$

Once the two current components are known, the total phase current at the time instant $k+1$ is computed as the sum of the magnetizing and iron loss currents. Then, i_m^{k+1} is used to extract torque and iron loss from their respective maps, and the Joule loss in the windings is computed using (8).

The results of the TSC simulation, with the pre-fault occuring at peak torque along the MTPA at the base speed, are reported in Fig. 10. The plots highlight the magnetizing current waveform and the flux linkage damping due to the losses. Regarding torque, oscillations are observed exceeding the maximum motor torque. Electromagnetic and mechanical losses are practically superimposed.

A. *Effect of the Pre-Fault Condition*

The pre-fault conditions heavily affect the TSC behavior, as disclosed in [10]. However, the pre-fault speed can heavily affect also the rotational loss terms that are a central point of this analysis. In the following, two pre-fault points are considered and compared: the first point is the maximum torque at base speed, controlling the motor along its Maximum Torque per Ampere (MTPA) locus. This represents the worst-case scenario among the possible pre-fault points, as it has the highest speed within the full flux linkage working points. The second condition is the no-load condition at maximum speed. Here, the effect of rotational loss is amplified, but it is not critical in terms of current, as the pre-fault flux linkage is lower.

Fig. 11 reports the comparison between these two operating points. As expected, the highest short-circuit current is obtained for the first point due to the higher flux linkage. Regarding the loss components, the DC-related losses are dominant for the first operating point, whereas they constitute slightly less than half of the total losses for the high-speed scenario. This observation underscores the limitation of neglecting rotational losses in the short-circuit model estimation.

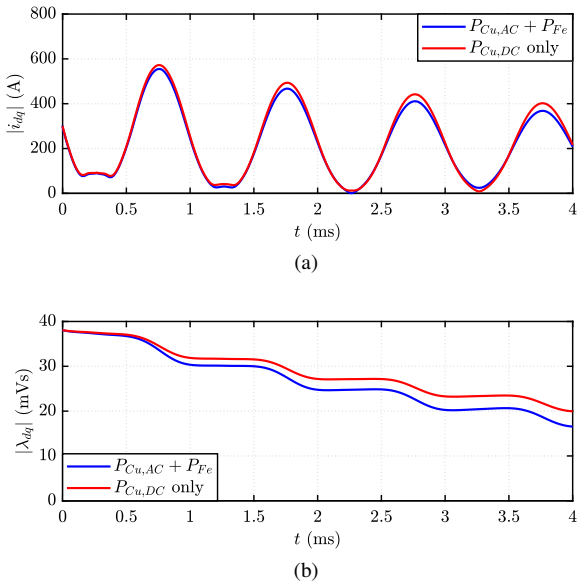


Fig. 12. Effect of loss on TSC behaviors: a) current amplitude and b) flux linkage versus time for the worst-case pre-fault point.

B. Comparison with DC Loss Model

To assess the effect of the rotational loss in the TSC waveform estimation, two evaluations are performed considering the most critical pre-fault point. The first evaluation considers all the loss components, while the second neglects all rotational losses, considering just the loss related to $R_{s,DC}$. The comparison is reported in Fig. 12 in terms of current, flux linkage and loss waveforms.

The first interesting point is that in the initial instants of the short-circuit, the contribution of rotational losses is minimal, leading to a slight overestimation (2%) of the peak short-circuit current when rotational losses are neglected. However, rotational losses increase the damping of the flux linkage, resulting in faster convergence to steady-state operation. After 4 electrical cycles, the flux linkage is 8% lower when rotational losses are considered. This difference becomes more evident at maximum speed.

C. Validation with Dynamic Model

A first validation of the proposed method is performed with dynamic simulation of the drive. The model is implemented in Simulink/SimScape and it is based on the same flux and loss maps. The speed is set constant and the pre-fault condition is the peak torque along MTPA at base speed. The aim of this first validation is to verify the computation process, since the model at the base is the same for both maps elaboration and dynamic model. The results in terms of dq currents, torque and dq flux linkages are reported in Fig. 13 and compared with the proposed magnetic model manipulation (MMM). The curves obtained with the maps elaboration and the dynamic model simulation are perfectly aligned, confirming the accuracy of the proposed elaboration process.

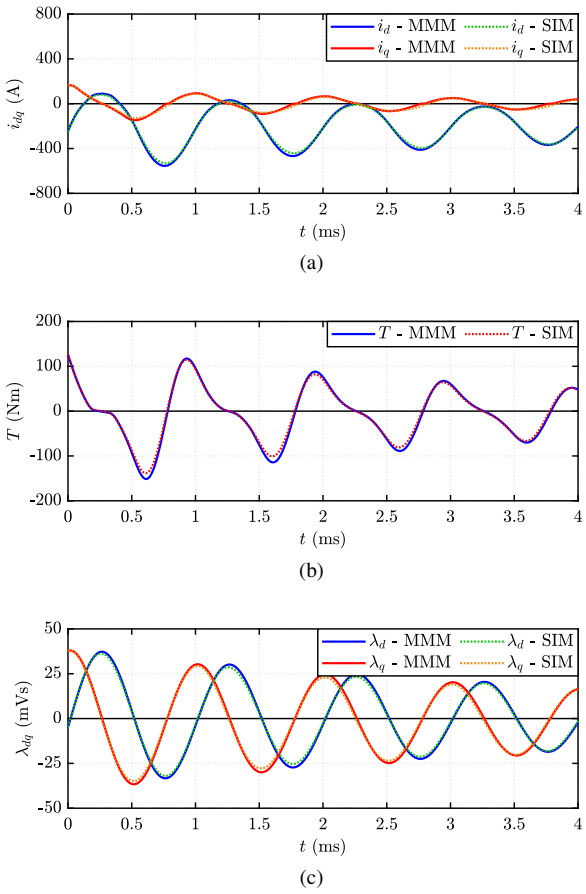


Fig. 13. Comparison between the proposed flux and loss maps elaboration (MMM) and the dynamic model simulation (SIM) in Simulink/SimScape environment at peak torque and base speed: a) dq current components, b) torque and c) dq flux linkage components function of time.

D. Validation with FEA Simulations

The proposed model is further validated against dedicated FEA simulations. The model is implemented in JMAG, considering all the loss terms. The short-circuit is imposed using the supply circuit and the peak torque at base speed selected as pre-fault point. The results from JMAG (FEA) and the proposed flux maps elaboration (MMM) are reported in Fig. 14, illustrating dq currents, flux linkages and torque. The comparison shows an almost perfect match between the proposed elaboration and FEA simulations. A notable difference is observed in the torque waveform, where torque ripple from the FEA simulation is evident, reflecting motor harmonic content not captured in the fundamental flux maps used in the proposed modeling. Furthermore, another significant difference between the proposed flux and loss maps based on elaboration and the FEA simulation is the computational time: the former takes approximately 12 seconds for the simulation of 5 electrical cycles as shown in the comparison, while the dedicated FEA simulation takes about 3 minutes.

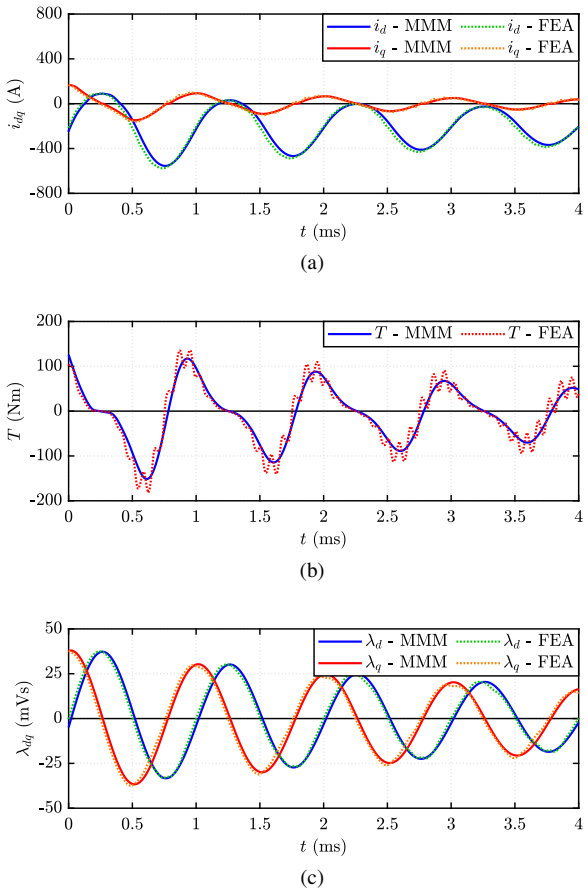


Fig. 14. Comparison between the proposed flux and loss maps elaboration (MMM) and dedicated FEA simulations at peak torque and base speed: a) *dq* current components, b) torque and c) *dq* flux linkage components function of time.

V. Conclusions

The paper presents a model for the estimation of short-circuit behaviors of PMSM. The method is based on flux maps, allowing a wide coverage of several kind of motors and accounts for AC-related winding loss and iron and PM loss, to improve the model accuracy, especially at high speeds. The model is adopted to investigate the short-circuit behaviors both in steady-state and during transient, highlighting that the rotational losses have a significant impact at high speeds and steady-state operation, while for low speeds and very short time intervals, the model neglecting iron loss can be considered accurate. Furthermore, the proposed magnetic model elaboration is validated against dynamic model simulation and dedicated FEA simulations, highlighting high accuracy of the proposed model and substantial computational time savings, compared to dynamic model (about 4 times faster) and especially dedicated FEA simulations (about 12 times faster). Finally, the presented model and analysis suggest that iron losses and AC-related losses can be disregarded when estimating peak short-circuit currents for very short-time frame, the additional damping offered from this loss terms is not sufficient to reduce the flux linkage amplitude and so the peak short-circuit current. On the other side, these losses must be considered when the steady-state short-circuit is studied, particularly in applications requiring motor resilience for fault tolerance, such as aerospace applications. Addressing these additional losses is crucial for accurate analysis and thermal management of the faulted system.

Acknowledgment

The research has been conducted with the support of Power Electronics Innovation Center (PEIC) of Politecnico di Torino (www.peic.polito.it).

References

[1] B. Ban, A. Kersten, A. Andersson, and S. Stipetic, "Metamodel-based design and optimization of a spoke-type interior permanent magnet machine for a vehicle traction application," in *2022 XIV International Symposium on Industrial Electronics and Applications (INDEL)*, 2022, pp. 1–6.

[2] R. R. Moghaddam, S. Nategh, J. Islam, and A. Boglietti, "Different traction motor topologies used in e-mobility : Part ii: Magnet-based solutions," in *2020 International Conference on Electrical Machines (ICEM)*, vol. 1, 2020, pp. 138–143.

[3] L. Di Leonardo, F. P. Collazzo, M. Villani, M. D'Andrea, C. D'Angelo, and M. Nucatola, "Permanent magnet synchronous machine for hybrid light aircraft," in *2022 International Conference on Electrical Machines (ICEM)*, 2022, pp. 1190–1196.

[4] N. Bianchi, D. Michieletto, L. Cinti, C. Contò, P. G. Carlet, M. Brunetti, and A. Nesci, "Permanent magnet synchronous motor drives for more-electric aircraft," in *2022 International Symposium on Power Electronics, Electrical Drives, Automation and Motion (SPEEDAM)*, 2022, pp. 871–876.

[5] A. Akay, P. Lefley, and M. Kansara, "Open-Circuit Fault-Tolerant Control for a Five-Phase Permanent Magnet Synchronous Machine Drive," in *2020 7th International Conference on Electrical and Electronics Engineering (ICEEE)*, Apr. 2020, pp. 150–154.

[6] C.-Z. Liaw, W. Soong, B. Welchko, and N. Ertugrul, "Uncontrolled generation in interior permanent-magnet machines," *IEEE Transactions on Industry Applications*, vol. 41, no. 4, pp. 945–954, 2005.

[7] A. Ruiz, A. Meseamanolis, L. Santolaria, M. Maleki, and A. Baschnagel, "Active Short Circuit Capability of HalfBridge Power Modules Towards EMobility Applications," in *PCIM Europe digital days 2021; International Exhibition and Conference for Power Electronics, Intelligent Motion, Renewable Energy and Energy Management*, May 2021, pp. 1–7.

[8] W. Wang, J. K. Nøland, P. K. Olsen, and S. W. Johannessen, "Optimal active short-circuit operation of permanent magnet synchronous machines and drives for aerospace applications," in *2024 International Conference on Electrical Machines (ICEM)*, 2024, pp. 1–7.

[9] W. Peng, W. Kun, and F. Meng, "Demagnetization study of permanent magnet machine under three phase short circuit," in *2023 IEEE 6th International Electrical and Energy Conference (CIEEC)*, 2023, pp. 2705–2710.

[10] S. Ferrari, G. Dilevrano, P. Ragazzo, P. Pescetto, and G. Pellegrino, "Fast determination of transient short-circuit current of pm synchronous machines via magnetostatic flux maps," *IEEE Transactions on Industry Applications*, vol. 59, no. 4, pp. 4000–4009, 2023.

[11] S. Ferrari, P. Ragazzo, G. Dilevrano, and G. Pellegrino, "Flux and loss map based evaluation of the efficiency map of synchronous machines," *IEEE Transactions on Industry Applications*, vol. 59, no. 2, pp. 1500–1509, 2023.

[12] S. Ferrari and G. Pellegrino, "SyR-e: Synchronous Reluctance (machines) - evolution." [Online]. Available: www.github.com/SyR-e